Probing dipole-forbidden autoionizing states by isolated attosecond pulses

Wei-Chun Chu,[1,2] Toru Morishita,[3] and C. D. Lin[1]

[1]*J. R. Macdonald Laboratory, Department of Physics, Kansas State University, Manhattan, Kansas 66506, USA*

[2]*Max Planck Institute for the Science of Light, Günther-Scharowsky-Straße 1, 91058 Erlangen, Germany*

[3]*Department of Engineering Science, The University of Electro-communications 1-5-1 Chofu-ga-oka, Chofu-shi, Tokyo 182-8585, Japan*

(Received 13 February 2014; published 27 March 2014)

We propose a general technique to retrieve the information of dipole-forbidden resonances in the autoionizing region. In the simulation, a helium atom is pumped by an isolated attosecond pulse in the extreme ultraviolet (EUV) combined with a few-femtosecond laser pulse. The excited wave packet consists of the ^1S, ^1P, and ^1D states, including the background continua, near the $2s2p(^1P)$ doubly excited state. The resultant electron spectra with various laser intensities and time delays between the EUV and laser pulses are obtained by a multilevel model and an *ab initio* time-dependent Schrödinger equation calculation. By taking the *ab initio* calculation as a "virtual measurement," the dipole-forbidden resonances are characterized by the multilevel model. We found that in contrast to the common assumption, the nonresonant coupling between the continua plays a significant role in the time-delayed electron spectra, which shows the correlation effect between photoelectrons before they leave the core. This technique takes the advantages of ultrashort pulses uniquely and would be a timely test for the current attosecond technology.

DOI: 10.1103/PhysRevA.89.033427 PACS number(s): 32.80.Zb, 32.80.Qk, 32.70.Cs

I. INTRODUCTION

Photoexcitation or photoionization processes are among the most common tools to study the structures of matters. For atomic or molecular systems, the details in the spectroscopy reveal the information at the microscopic regime such as the energy levels, decay rates, and transition strengths between the quantum states. A large amount of data has been obtained and recorded by synchrotron radiations up to the x-ray regimes. Due to the limited brilliance of the light sources, or the limited intensity of the fields, normally only single-photon processes are considered in synchrotron measurements. Although it can be very precise and reliable to obtain the atomic energy levels, the dipole-forbidden states (DFSs) with respect to the ground state are not accessible. Nonetheless, these DFSs are essential in numerous optical techniques or subjects including electromagnetically induced transparency (EIT) [1,2], two-photon absorption [3,4], Raman spectroscopy, and more. It is noteworthy that some of these or similar quantum phenomena have been reconsidered in ultrafast optical configurations [5–9] and attract much attention, where their interpretations are based on the dynamics involving DFSs. Until now the aspiration for better measurements or characterizations of DFSs is tremendous.

In recent years, there are renewed interests in the studies of Fano resonances and the corresponding autoionizing states (AISs), which have long been perceived in the energy domain as interpreted by Fano more than 50 years ago [10]. The new interests are founded on the developments in ultrashort light sources and ultrafast optical techniques. The EIT effect between the coupled AISs was observed by time-delayed transient absorption in the femtosecond timescale [7]. The time-domain measurements of the autoionization dynamics using attosecond pulses were reported in argon [11] and in helium [12]. Most recently, the Fano line shapes modulated by time-delayed intense fields in transient absorption spectroscopy have been measured and analyzed [8,9], which has also brought to light the astounding potential to shape and to control the attosecond pulses [13]. In these studies and the related theoretical works, the dynamics of the Fano wave packet were mostly implemented as attosecond streaking [14,15] or resonant coupling [16–19] of the Fano states, if not carried out by *ab initio* calculations [20–22], which were numerically expensive and less intuitive. While the attention has been put on the directly measurable resonances under the dressing field, the properties of the dipole-forbidden resonances (DFRs) in the coupling were largely overlooked. In this work, we aim to provide a model describing the realistic coupling between the AISs where the DFRs can be "probed," and their essential properties can be characterized.

Taking the helium atom in the energy range near the $2s2p(^1P)$ resonance as an example, we carry out an *ab initio* two-active-electron time-dependent Schrödinger equation (TAE-TDSE) based on the time-dependent hyperspherical (TDHS) method [23–25] to virtually provide the reference experimental data. Then a multilevel model with parametrized atomic structure is developed and applied to the case, where the comparison to the virtual experiment optimizes the atomic parameters of the DFRs. In our previous model consisting of coupled AISs [19], the transitions between the AISs were reduced to the transitions involving only the bound states—bound-bound (B-B) transitions—by ignoring the second-order (two-electron) transitions. This naive picture successfully predicted the inversion of Fano line shapes under intense dressing fields, but the effects on the DFRs were missing. The present model includes the transitions between the discrete states and the background continua (bound-continuum, B-C), and between the background continua of different symmetries (continuum-continuum, C-C). With ultrashort dressing fields, the significance of the B-C and C-C transitions is justified because these transitions take place in such a short time when electrons are still near the ionic core, and the distorted continuum waves are far from plane waves. This improved picture emphasizes the influences of these added transitions in the dressing field on the Fano line shapes of all resonances, including the DFRs. This signature broadly implies that in ultrafast dynamics, even in weak fields in the sense of few-photon

transitions, the implementation or neglection of the C-C transitions needs to be reconsidered carefully, especially for ultrashort overlapping pulses.

The structure of this article is in the following. Section II gives detail accounts of the formulation of the present model for the multilevel autoionizing systems and its differences from previous models. The limitation of the current model is discussed. Section III A connects the laser-dressed angle-resolved electron spectroscopy—the preassumed measurement—to the retrieval of the parameters in the model. Section III B compares the calculations by the present model and by TAE-TDSE to determine the atomic parameters. Using the present model with the retrieved parameters, Sec. III C presents the time-delayed electron spectra by the synchronized attosecond extreme ultraviolet (EUV) and strong laser pulses, as such a scheme is commonly performed experimentally to extract the ultrafast dynamics. The role of the C-C coupling in the model is elaborated in Sec. III D. Finally, Sec. IV gives the concluding remarks. In this paper, we use eletron volts (eV) and femtoseconds (fs) except in Sec. II, unless otherwise specified. Field intensity is defined by the cycle-averaged values.

II. MODEL

The present model describes the dynamics of an autoionizing wave packet in an atom consisting of the AISs of two different symmetries, which are pumped by a weak EUV attosecond pulse and dressed by a relatively strong (TW/cm^2) femtosecond laser pulse. The goal is to calculate the photoelectron spectrum with a given set of fields and atomic parameters. Providing the angular distribution of the electrons in real measurements, we assume that the spectrum of each spherical partial wave can be isolated. The separation of partial waves in the experimental point of view will be further discussed in Sec. III. Each partial wave is then compared with the result from the TAE-TDSE calculation, which is described in details in Refs. [24,25]. By optimizing the modeled spectra, the atomic parameters are retrieved. In this section, atomic units (a.u.) are used unless otherwise specified.

The autoionizing system pumped by the EUV and strongly coupled by the laser is schematically plotted in Fig. 1. The total wave function of the atomic system is written as

$$|\Psi(t)\rangle = e^{-i\epsilon_g t} c_g(t)|g\rangle + e^{-i\epsilon_e t}\left[\sum_m c_m(t)|m\rangle + \int c_{\epsilon_1}(t)|\epsilon_1\rangle d\epsilon_1 + \sum_n c_n(t)|n\rangle + \int c_{\epsilon_2}(t)|\epsilon_2\rangle d\epsilon_2\right], \quad (1)$$

where $|g\rangle$ is the ground state with energy ϵ_g, and $\epsilon_e \equiv \epsilon_g + \omega_X$ corresponds to the central energy level pumped by the EUV, where ω_X is the photon energy of the EUV. The fast oscillation in terms of the EUV frequency is factored out, where the $c(t)$ coefficients are slowly varying in time. The bound excited states $|m\rangle$ and $|n\rangle$ are embedded in the background continua $|\epsilon_1\rangle$ and $|\epsilon_2\rangle$, respectively, where the labels $|m\rangle$ and $|\epsilon_1\rangle$ are used exclusively for dipole-allowed states, and $|n\rangle$ and $|\epsilon_2\rangle$ are used exclusively for dipole-forbidden states. The Hamiltonian

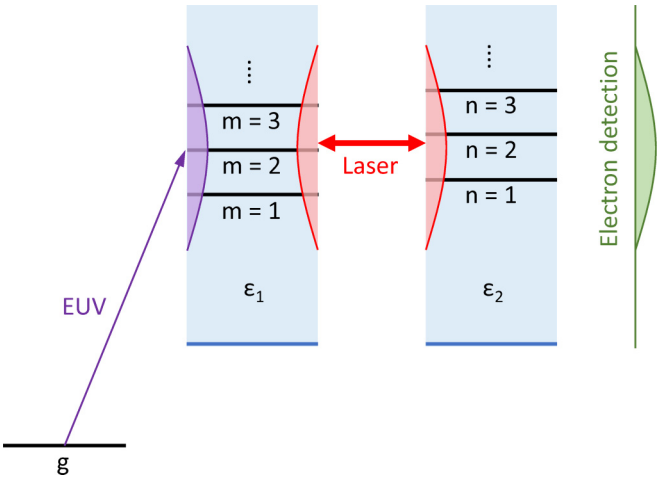

FIG. 1. (Color online) Schematics of the coupled autoionizing system. The purple and red arrows are the transitions by the EUV and laser pulses. The bandwidths of the EUV covers a group of AISs $|m\rangle$ and the background continuum $|\epsilon_1\rangle$. The laser couples $|m\rangle$ and $|\epsilon_1\rangle$ to states of other symmetries by single-photon transitions following the selection rule. The final wave packet after the pulse is projected out in the photoelectron spectroscopy.

of the system is $H(t) = H_A - [E_X(t) + E_L(t)]\,D$, where H_A is the atomic Hamiltonian, $E_X(t)$ and $E_L(t)$ are the electric fields of the EUV and the laser, respectively, and D is the dipole operator. Thus, in this basis set, the off-diagonal elements in the Hamiltonian are

$$\langle g|H|m\rangle = -D_{gm}E_X(t), \quad (2)$$
$$\langle g|H|\epsilon_1\rangle = -D_{g\epsilon_1}E_X(t), \quad (3)$$
$$\langle m|H|n\rangle = -D_{mn}E_L(t), \quad (4)$$
$$\langle m|H|\epsilon_2\rangle = -D_{m\epsilon_2}E_L(t), \quad (5)$$
$$\langle \epsilon_1|H|n\rangle = -D_{\epsilon_1 n}E_L(t), \quad (6)$$
$$\langle \epsilon_1|H|\epsilon_2\rangle = -D_{\epsilon_1\epsilon_2}E_L(t), \quad (7)$$

for the dipole transitions, and

$$\langle m|H|\epsilon_1\rangle = V_{m\epsilon_1}, \quad (8)$$
$$\langle n|H|\epsilon_2\rangle = V_{n\epsilon_2}, \quad (9)$$

for the configuration interactions responsible for autoionization, and D and V are determined by the atomic structure. Note that the dimensions of the Hamiltonian matrix elements are ϵ, $\sqrt{\epsilon}$, and 1 for B-B, B-C, and C-C transitions, respectively, where ϵ denotes energy. For simplicity, we employ the standing wave representation for the continuum states in Eq. (1), so all D and V are real quantities.

Certain approximations are adopted to simplify the model. The type of measurement in our concern involves a perturbative EUV pulse with the bandwidth of a few eVs, and a few-cycle laser pulse in the infrared to visible energy region and with the intensity up to the TW/cm^2 scale. The EUV field is written in the form of

$$E_X(t) = F_X(t)e^{i\omega_X t} + F_X^*(t)e^{-i\omega_X t}, \quad (10)$$

where $F_X(t)$ is the field envelope containing any additional phase other than the carrier phase. The rotating wave approximation (RWA) can be applied to the EUV, where for each

transition, only one of the two terms in Eq. (10) is taken into account. For the laser pulse, RWA is not suitable since the bandwidth for a few-cycle pulse is comparable to its central frequency. The wave packet is in the energy range much higher than the binding energy so that the background continua change only slightly across each resonance, where the D and V elements are constants of energy estimated at each resonance. In the following derivation, the energy dependence of D and V is kept in the expression for clarity if necessary, but is removed in the numerical evaluation.

By solving TDSE with the total wave function in Eq. (1), the equation of motion (EOM), or the coupled equations for all the $c(t)$ coefficients can be established. By applying adiabatic eliminations (AE) of the continua, i.e., assuming $\dot{c}_{\epsilon_1}(t) = \dot{c}_{\epsilon_2}(t) = 0$ in the original coupled equations for the continuum, the preliminary forms of the continuum-state coefficients are obtained as

$$c^p_{\epsilon_1}(t) = \frac{1}{\delta_{\epsilon_1}}\Bigg[-F^*_X(t)D_{\epsilon_1 g}c_g(t) + \sum_m V_{\epsilon_1 m}c_m(t) - E_L(t)\sum_n D_{\epsilon_1 n}c_n(t)\Bigg], \tag{11}$$

$$c^p_{\epsilon_2}(t) = \frac{1}{\delta_{\epsilon_2}}\Bigg[\sum_n V_{\epsilon_2 n}c_n(t) - E_L(t)\sum_m D_{\epsilon_2 m}c_m(t)\Bigg], \tag{12}$$

where $\delta_1 \equiv \epsilon_e - \epsilon_1$ and $\delta_2 \equiv \epsilon_e - \epsilon_2$ are the detuning of the continuum states. With the assumption $c_g(t) = 1$ for the perturbative EUV, the preliminary forms are then inserted back to the EOM, which gives the coefficients of the bound excited states by

$$i\dot{c}_m(t) = -F^*_X(t)\bar{D}_{mg} - (\delta_m + i\kappa_m)c_m(t) - E_L(t)\sum_n \bar{D}_{mn}c_n(t), \tag{13}$$

$$i\dot{c}_n(t) = -iF^*_X(t)E_L(t)j_{ng} - (\delta_n + i\kappa_n)c_n(t) - E_L(t)\sum_m \bar{D}_{nm}c_m(t), \tag{14}$$

where $\delta_m \equiv \epsilon_e - \epsilon_m$ and $\delta_n \equiv \epsilon_e - \epsilon_n$ are the detuning of the AISs, $\kappa_m \equiv \Gamma_m/2 = \pi|V_{m\epsilon_1}|^2$ and $\kappa_n \equiv \Gamma_n/2 = \pi|V_{n\epsilon_2}|^2$ are the half widths of the resonances, and $j_{gn} \equiv \pi D_{g\epsilon_1}D_{\epsilon_1 n}$ is the light-induced broadening of the DFRs. The composite dipole matrix elements $\bar{D}$ are defined by

$$\bar{D}_{gm} \equiv D_{gm} - i\pi D_{g\epsilon_1}V_{\epsilon_1 m}, \tag{15}$$

$$\bar{D}_{mn} \equiv D_{mn} - \pi^2 V_{m\epsilon_1}D_{\epsilon_1\epsilon_2}V_{\epsilon_2 n} - i\pi\left(V_{m\epsilon_1}D_{\epsilon_1 n} + D_{m\epsilon_2}V_{\epsilon_2 n}\right). \tag{16}$$

The elements $\bar{D}_{gm}$ and $\bar{D}_{mn}$ are responsible for the EUV and laser transitions, respectively. For a given $\bar{D}_{gm}$, the Fano q parameter of the $|m\rangle$ state is easily identified as

$$q_m = \frac{D_{gm}}{\pi D_{g\epsilon_1}V_{\epsilon_1 m}}. \tag{17}$$

For each dipole-allowed state $|m\rangle$, q_m only takes the EUV transition from the ground state into account, and is the commonly known and measured Fano line shape parameter. On the other hand, for each DFR $|n\rangle$, the q parameter needs to consider the laser transitions from all possible paths, and to represent the phase induced by the interference between the autoionization paths and the direct ionization paths. Each $\bar{D}_{mn}$ counts only one pair of $|m\rangle$ and $|n\rangle$ states, and the general line shapes of $|n\rangle$ is determined by the collection of $\bar{D}_{mn}$ of all m under the laser bandwidth. As one of the approximations, because the structures of the background continua change sufficiently slowly in the energy ranges in concern, Γ_m, Γ_n, $\bar{D}_{gm}$, $\bar{D}_{mn}$, q_m, and j_{gn} are constant of energy estimated just at the single energy points $\epsilon_1 = \epsilon_m$ and $\epsilon_2 = \epsilon_n$, except that j_{gn} is estimated at $\epsilon_1 = \epsilon_e$.

After the calculation of the bound-state coefficients $c_m(t)$ and $c_n(t)$, we aim to recover the continuum-state coefficients $c_{\epsilon_1}(t)$ and $c_{\epsilon_2}(t)$ from the preliminary forms. Note that AE works for the treatment in Eqs. (13) and (14) because only the collective effects by the continua are needed there, which are not strongly affected by the detail shapes of the continua. Here, when the goal is to acquire the electron spectra, we have to go beyond AE and keep the previously eliminated terms, i.e., $i\dot{c}_{\epsilon_1}(t)/\delta_{\epsilon_1}$ and $i\dot{c}_{\epsilon_2}(t)/\delta_{\epsilon_2}$, in $c^p_{\epsilon_1}(t)$ and $c^p_{\epsilon_2}(t)$, respectively. The corrected preliminary forms are then employed in the mutual coupling terms between the continua to finally obtain

$$i\dot{c}_{\epsilon_1}(t) = -F^*_X(t)D_{\epsilon_1 g} - \delta_{\epsilon_1}c_{\epsilon_1}(t) + \sum_m V_{\epsilon_1 m}c_m(t) - E_L(t)\left[\sum_n \bar{D}_{\epsilon_1 n}c_n(t) + \alpha_{\epsilon_1}(t)\right], \tag{18}$$

$$i\dot{c}_{\epsilon_2}(t) = -iF^*_X(t)E_L(t)j_{\epsilon_2 g} - \delta_{\epsilon_2}c_{\epsilon_2}(t) + \sum_n V_{\epsilon_2 n}c_n(t) - E_L(t)\left[\sum_m \bar{D}_{\epsilon_2 m}c_m(t) + \alpha_{\epsilon_2}(t)\right], \tag{19}$$

where the composite dipole matrix elements therein are defined by

$$\bar{D}_{\epsilon_1 n} \equiv D_{\epsilon_1 n} - i\pi D_{\epsilon_1\epsilon_2}V_{\epsilon_2 n}, \tag{20}$$

$$\bar{D}_{m\epsilon_2} \equiv D_{m\epsilon_2} - i\pi V_{m\epsilon_1}D_{\epsilon_1\epsilon_2}. \tag{21}$$

The direct coupling terms between the continua (not via any resonances), given by

$$\alpha_{\epsilon_1}(t) \equiv \pi D_{\epsilon_1\epsilon_2}\dot{c}_{\epsilon_2}(t)\big|_{\epsilon_2=\epsilon_e}, \tag{22}$$

$$\alpha_{\epsilon_2}(t) \equiv \pi D_{\epsilon_1\epsilon_2}\dot{c}_{\epsilon_1}(t)\big|_{\epsilon_1=\epsilon_e}, \tag{23}$$

are calculated in each time step by Eqs. (18) and (19) without the $\alpha(t)$ terms, and they are then added back as iterative corrections. The coupling between the continua through $\alpha(t)$ greatly reduce the number of coupled equations in the numerical calculation from $2N^2$ to $2N$, where N is the number of energy steps in the range in concern. An 8-eV wide wave packet with the energy resolution of 20 meV will require $N = 400$, which is typical for an IAP + IR excitation. The validity of the $\alpha(t)$ terms relies on the smoothness of the continuum coefficients, which makes possible a simple collective effect for the other continuum in the coupling.

By Eqs. (13), (14), (18), and (19), and with a given set of atomic and field parameters, the total wave function in the form of Eq. (1) is uniquely determined. The electron spectra for the two symmetries are $P_1(\epsilon_1) = |c_{\epsilon_1}(t_f)|^2$ and $P_2(\epsilon_2) = |c_{\epsilon_2}(t_f)|^2$ where t_f is much larger than all the resonance lifetimes after the coefficients are stablized [16]. Alternative to Eq. (1), the total wave function can also be written in atomic eigenstates, where the coefficients $\bar{c}_{\epsilon_1}(t_f)$ and $\bar{c}_{\epsilon_2}(t_f)$, associated with the two symmetries, respectively, are stabilized right after the end of the external field. Thus, in cases with ultrashort pulses, employing the form of the total wave function in eigenstate basis cuts down the calculation time significantly. The conversion between the eigenstate coefficients and the bound-state and continuum-state coefficients has been detailed in Ref. [16] and is given by

$$\bar{c}_\epsilon(t) = (i\sin\theta_\epsilon - \cos\theta_\epsilon)\, c_\epsilon(t) + \cos\theta_\epsilon \sum_l \frac{\tan\theta_{\epsilon l}}{\pi V_l} c_l(t), \tag{24}$$

where

$$\tan\theta_{\epsilon l} \equiv -\frac{\kappa_l}{\epsilon - \epsilon_l} \tag{25}$$

and

$$\tan\theta_\epsilon \equiv \sum_l \tan\theta_{\epsilon l}, \tag{26}$$

where ϵ and l are the indices belonging to the same symmetry (ϵ_1, m or ϵ_2, n in the present case).

The inclusion of the laser coupling involving continuum states, particularly the C-C transitions that have been ignored previously, raises the dressing intensities that could be handled properly. Nonetheless, we should stress the restrictions of this model in the following. First of all, the model works only in the presence of bound states on both sides of the coupling. The assumption that the continua evolve more slowly than the bound states is required for AE, which relies on the existence of near-resonant bound states to mediate all transitions. Second, the description of the system is in terms of atomic angular momentum eigenstates, which is not suitable for the strong field ionization in the streaking regime [26]. In such a regime, the momentum of emitted electrons are shifted in the direction parallel to the polarization of field, so that the wave packet in general consists of a large number of angular momenta.

III. RESULTS AND ANALYSIS

A. Partial wave analysis of photoelectrons

We apply the general technique described above to the simplest autoionizing system, helium atom, in the energy range centered at the lowest dipole-allowed doubly excited state $2s2p(^1P)$ (referred by $2s2p$ hereafter). With linearly polarized EUV and laser pulses and following the selection rules, the final detected photoelectron wave packet is composed by $^1S^e$, $^1P^o$, and $^1D^e$ states of magnetic quantum number $m = 0$, under the constraint that the laser intensity is within the limit of 1 TW/cm^2 so that other symmetries are negligible. Thus following the same derivation introduced in the model, the third symmetry is included in the coupled equations, and its coefficients are solved accordingly.

The excited wave packet $|\Psi_E(t)\rangle$, consisting of the excited bound and continuum states as defined in Eq. (1), is written as

$$|\Psi_E(t)\rangle = e^{-i\epsilon_e t} \sum_{l=0}^{2} \int \bar{c}_{\epsilon l}(t)|\epsilon l\rangle d\epsilon, \tag{27}$$

where $|\epsilon l\rangle$ are the atomic eigenstates with electron energy ϵ and angular momentum l, following the conventional atomic orbital notations. Note that in this expression, the core orbital is skimmed because in our case and the energy range in concern, the core orbital is always $1s$ (the excitation energy of $2s$ and $2p$ from the ionic ground state is 40.8 eV, which is 5.3 eV higher than the $2s2p$ level). The angular momentum of the photoelectron in the s, p, or d partial wave is already the total angular momentum. The symmetry in the model description is directly mapped onto the angular momentum of the photoelectron in the present calculation. The shorthands S, P, and D are used hereafter for the three symmetries of the total wave function in concern.

For detecting photoelectrons with angular distribution, the wave packet in Eq. (27) should be projected onto the final state of momentum $\vec{k}$ that satisfies incoming boundary conditions and represents the ejected photoelectron [27]. In particular, it is written in the energy-normalized form by

$$\psi_{\vec{k}}^{(-)}(\vec{r}) = \sqrt{\frac{2}{\pi k}} \frac{1}{r} \sum_{lm} i^l e^{-i\eta_l} u_l(kr) Y_l^m(\hat{r}) Y_l^{m*}(\hat{k}), \tag{28}$$

where η_l are the total phase shift due to the atomic potential and $u_l(kr)$ are the radial waves corresponding to $|\epsilon l\rangle$. The measured signal is $P(\vec{k}) = |\langle\psi_{\vec{k}}^{(-)}|\Psi_E(t_f)\rangle|^2$, where t_f is the detection time, which is infinite after the ionization in the atomic timescale. The angle- and energy-resolved electron yield, corresponding to the $\vec{k}$ component of the wave packet, is thus

$$\begin{aligned} P(\epsilon,\theta) &= |\langle\psi_{\vec{k}}^{(-)}|\Psi_E(t_f)\rangle|^2 \\ &= \left|\sum_{l=0}^{2} \sqrt{\frac{2l+1}{4\pi}} \frac{e^{i\eta_l}}{i^l} \bar{c}_{\epsilon l}(t_f) P_l(\cos\theta)\right|^2, \end{aligned} \tag{29}$$

where $\epsilon = k^2/2$, θ is the polar angle of the momentum direction $\hat{k}$ with respect to the polarization of fields, and the azimuth dependence has been removed by considering only $m = 0$.

In the above, we have described how the electron yield $P(\epsilon,\theta)$ is related to the final wave packet of each partial wave expressed by $e^{i\eta_l}\bar{c}_{\epsilon l}(t_f)$. Nonetheless, with $P(\epsilon,\theta)$ given by a photoelectron measurement, the process to assign $e^{i\eta_l}\bar{c}_{\epsilon l}(t_f)$ should be achieved by numerical fitting with caution. In the current case, for each energy point, the three complex coefficients corresponding to $l = 0, 1, 2$ are fitted for the signal intensity as a function of θ. The energy range in concern is far above the binding energy, and the energy dependence of the phase of $e^{i\eta_l}\bar{c}_{\epsilon l}(t_f)$ is significant only across the resonances. In our case, the phase of $e^{i\eta_2}\bar{c}_{\epsilon d}(t_f)$ is set as an arbitrary constant of ϵ since there are no $l = 2$ resonances in this energy range. In this way, the coefficients of all partial waves in the whole energy region in concern are extracted from the experiment, i.e., we convert $P(\epsilon,\theta)$ to $e^{i\eta_l}\bar{c}_{\epsilon l}(t_f)$ as the main experimental data to be compared with.

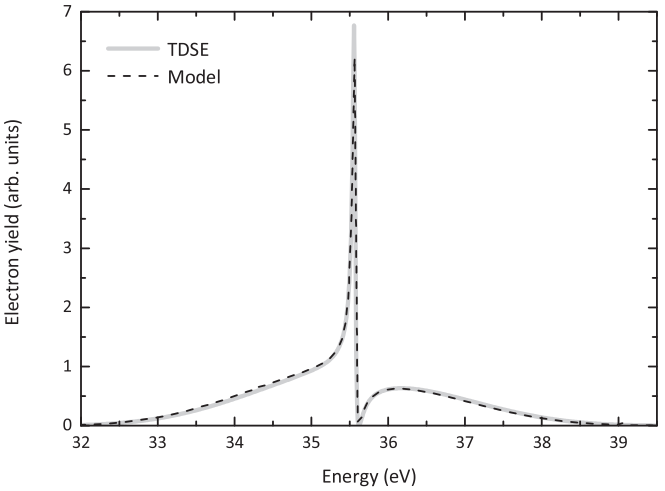

FIG. 2. Photoionization electron spectra near the He $2s2p$ resonance by a 690-as EUV pulse, calculated by TAE-TDSE and by the multilevel model. The EUV pump is weak, and only the p partial wave is nonnegligible. The energy, width, and q parameter of the resonance are retrieved by fitting with the TAE-TDSE.

B. Retrieval of atomic structure parameters

In the following, the TAE-TDSE calculation is taken as a virtual experiment, and the parameters in the model calculation are adjusted to achieve the best agreement. Since TAE-TDSE calculates photoelectron spectra in partial waves, the step to "dissemble" the measured signal into partial waves described in Sec. III A is skipped in our comparison to TAE-TDSE. In the physical process, a weak broadband EUV pulse is applied first to ionize the system. The duration is 690 as and the peak intensity is 10^9 W/cm^2. It excites a wave packet consisting of the $2s2p$ AIS and the $1s\epsilon p$ continuum about 4 eV wide around the resonance. In this laser-free condition, any states with symmetries other than P are negligible. The TAE-TDSE result of the electron spectrum is shown in Fig. 2 by the gray solid curve. The $2s3p(^1P)$ resonance appearing at 39.1 eV is very weakly pumped and neglected in this study. With only the TAE-TDSE result, the Fano parameters can already be characterized by the Fano line shape formula [10]

$$\sigma(\epsilon) = \sigma_0 \frac{(q+\epsilon)^2}{1+\epsilon^2}, \tag{30}$$

combined with the bandwidth profile of pulse, where $\epsilon \equiv 2(E - E_r)/\Gamma$ is the photon energy relative to the resonance energy E_r and normalized by the width Γ. Thus $\Gamma = 41$ meV and the line shape $q = -2.66$ for the $2s2p$ resonance are extracted. The obtained parameters agree well with the actual experimental values $\Gamma = 37$ meV and $q = -2.75$ [28]. Note that E_r in the model can be arbitrarily shifted by the binding energy and is not uniquely defined. With such parameters, the multilevel model reproduces the lineshape very well. By fitting the overall signal strength with TAE-TDSE, the absolute values of the dipole matrix elements $D_{1s^2,2s2p} = 0.036$ a.u. and $D_{1s^2,\epsilon_p} = -0.278$ a.u. are also obtained, where the ratio between them is already determined by q. This retrieval process relies on the frequency profile of the EUV pulse, which should be considerably wider than the resonance width and very smooth in frequency. A high-quality isolated attosecond pulse could do the job well.

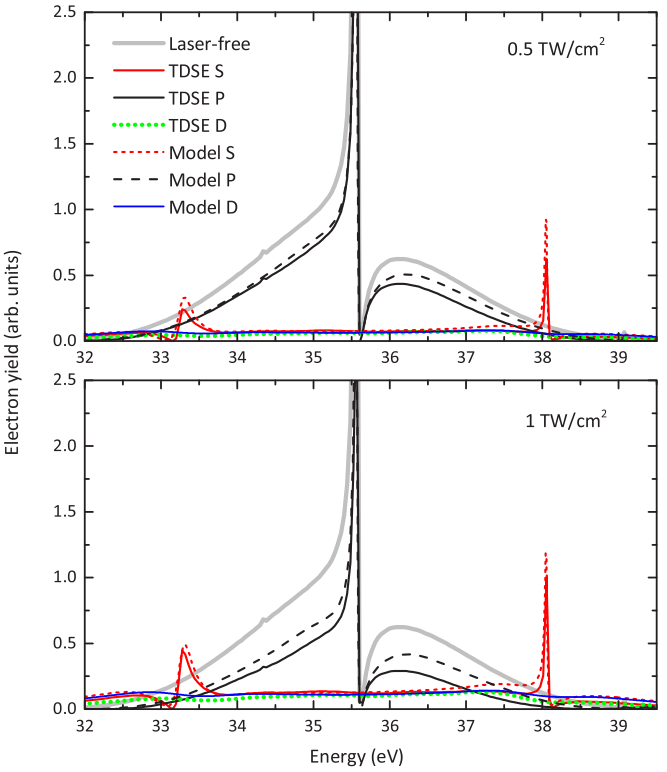

FIG. 3. (Color online) Laser-dressed EUV electron spectra of the dominant partial waves for the peak laser intensities of 0.5 and 1 TW/cm^2, calculated by TAE-TDSE and the multilevel model. For such moderately intense dressing fields, ϵp still surpasses, while ϵs and ϵd increase with the intensity of the dressing field. The atomic parameters in the model calculation are optimized for best agreement in the $I_0 = 0.5$ TW/cm^2 case. When the laser intensifies, more signals are "lost" due to the ionization by the laser, which is not counted by the multilevel model and responsible for the discrepancies in the comparison to the TAE-TDSE results.

In the presence of the laser pulse, the wave packet promoted by the EUV is distorted and projected onto a combination of symmetries of bound and continuum states. Nevertheless, in the intermediate intense laser, P is still the dominant symmetry, followed by S and D. For overlapping EUV and laser pulses, i.e., in the time delay $t_0 = 0$ condition (t_0 is defined by the temporal shift between the two pulse peaks and is positive when the EUV comes first), the electron spectra by TAE-TDSE of the dominant partial waves are shown in Fig. 3. The laser pulse is 4-fs (FWHM) long with the central wavelength of 540 nm, which corresponds to the central frequency of $\omega_L = 2.3$ eV. The carrier-envelope phase is set to 0, which means that at $t_0 = 0$, the EUV is at the maximum of the laser field in the positive polarization direction. The top and bottom panels of the figure are for peak laser intensities $I_0 = 0.5$ and 1 TW/cm^2, respectively. Two resonances clearly show up in ϵs at about 33.3 and 38.1 eV while ϵd is spectrally flat. These resonances have been reported in earlier works [29–31] and are identified as $2s^2(^1S)$ and $2p^2(^1S)$ (referred by $2s^2$ and $2p^2$ hereafter), respectively. We note that $2p^2(^1D)$ at

35.3 eV [31] is not excited by the laser pulse considered here, so it is not taken into account in the following analysis.

To retrieve the parameters of the dipole-forbidden states, we take the $I_0 = 0.5$ W/cm^2 case in Fig. 3 as the reference. In the region between 34 and 37 eV where no resonances are involved, the C-C dipole matrix elements $D_{\epsilon p,\epsilon s}$ and $D_{\epsilon p,\epsilon d}$ control the absolute signal strengths of ϵs and ϵd exclusively. The fitting gives $D_{\epsilon p,\epsilon s} = 29$ a.u. and $D_{\epsilon p,\epsilon d} = 27$ a.u. For the resonances $2s^2$ and $2p^2$, three parameters for each resonance are extracted at the same time by fitting its line shape, which are $\Gamma_{2s^2} = 225$ meV, $D_{2s2p,2s^2} = 1.5$ a.u., and $D_{1s\epsilon p,2s^2} = 2$ a.u. for $2s^2$ and $\Gamma_{2p^2} = 35$ meV, $D_{2s2p,2p^2} = 1.8$ a.u., and $D_{1s\epsilon p,2p^2} = 2$ a.u. for $2p^2$. The signals surrounding $2s^2$ and $2p^2$–most significantly at 37.5 and 38.5 eV–form small bumps away from the resonances, which further determine $D_{2s2p,1s\epsilon s} = 1$ a.u. The ϵd spectrum is quite insensitive to $D_{2s2p,1s\epsilon d}$ which can be set as 0. Now all the atomic structure parameters have been obtained. We keep the same parameters for further simulations with arbitrary dressing fields. As seen in the bottom panel of Fig. 3, as the laser intensifies, the ϵp spectrum decreases, and the ϵs and ϵd spectra, including the resonance part and the background part, increase. This means that the laser transfers the electrons from the $2s2p$ resonance–including its background continuum–to the S and D states, mainly by single-photon transitions.

With the same set of parameters, which have been retrieved in the $I_0 = 0.5$ TW/cm^2 case, the discrepancy between the multilevel model and TAE-TDSE grows with the dressing field intensity, as seen in Fig. 3. It is especially obvious in the depletion of the ϵp spectrum. This discrepancy comes from the laser ionization of the wave packet, which is not considered by our model. For the ionization from $2s2p$ to $2l\epsilon l'$, with the binding energy $I_p = 5.3$ eV, the central laser frequency $\omega_L = 2.3$ eV, and the peak laser intensity $I_0 = 0.5$ TW/cm^2, the Keldysh parameter ($\gamma = \sqrt{2I_p}\omega_L/E_0$ where E_0 is the peak field strength) is 13.8. This means that multiphoton ionization prevails over tunnel ionization. Considering the binding energies of $2s2p$, $2s^2$, and $2p^2$, their multiphoton ionization processes are at least third-order. Thus with the present laser intensities, the multiphoton ionization should not overpower the coupling between the resonances, and will not change the conclusion of this technique. The precise calculation of ionization rate of doubly excited states is a research field of its own and beyond the scope of this report.

C. EUV-plus-VIS spectroscopy

To study the dynamic optical response of the system, instead of tuning the laser intensity, experimentally it is easier to scan the time delay between the pulses while keeping the intensity the same. With the fixed $I_0 = 0.5$ TW/cm^2 and the detector direction at 0 degree (along the positive polarization direction of light), the angular-differential time-delay electron spectra by the multilevel model are shown in Fig. 4. In the time delay range where EUV and laser overlap and in the energy range between $2s^2$ and $2p^2$, the interference pattern forms fringes along the energy axis, which oscillate in the time delay in the period of the laser optical cycle (1.8 fs). When the EUV is at the zeros of the laser field (e.g., $t_0 = 0.9$ fs), the spectrum is slightly deviated from the $2s2p$ line shape, and

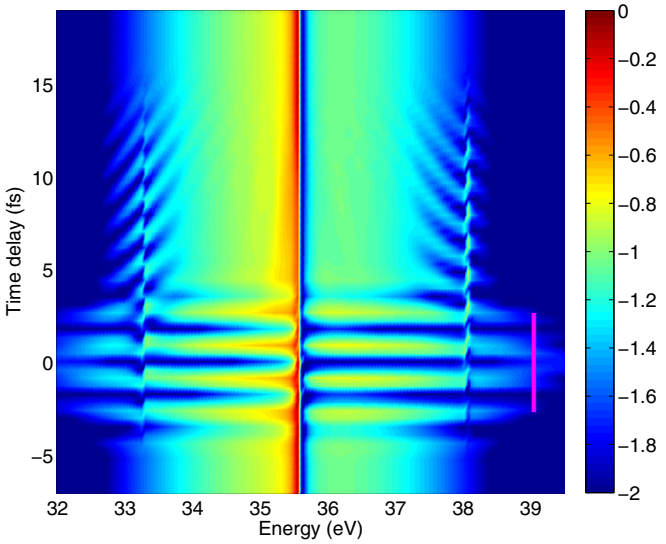

FIG. 4. (Color online) Angular differential electron spectra in the forward direction along the polarization by the model calculations. The signals are normalized and plotted in log scale (color bar is labeled by $\log_{10}\sigma$ where σ is the signal strength) with 20 dB dynamic range. The same parameters in Fig. 3 are applied, but with fixed laser intensity ($I_0 = 0.5$ TW/cm^2). The fringes near the overlap of the pulses form streakinglike patterns. The signals corresponding to the $2s^2$ and $2p^2$ resonances form sidebandlike structures. The magenta bar on the right indicates the pulse length (FWHM) of the dressing laser.

the bright fringes appear. When the EUV is on top of the local maximum of the laser field (e.g., $t_0 = 1.8$ fs), the P-state wave packet excited by the EUV is distorted, and a large portion of photoelectrons are transferred to the S and D states. The final wave packet in momentum is less directional in z, which results in the dark fringes. As stated in Sec. II, streaking effect is based on the linear momentum shift of the electrons and should be described by high angular momentum states in the spherical coordinates. Since the present model considers the angular momentum only up to $L = 2$, it is intrinsically incapable of quantitatively describing the streaking effect.

To further illuminate the atomic response near $t_0 = 0$ in terms of coupled partial waves, we show the ϵs spectra calculated by TAE-TDSE and by the multilevel model for small time delays in Fig. 5. The results agree well between the calculations. A clear feature seen in the figure is that the middle flat part of the spectrum oscillates alone t_0 with roughly half optical cycles (0.9 fs). In Fig. 4, with the alternating phase, ϵs is coherently added to ϵp to give the interference pattern oscillating in full optical cycles. On the contrary, the ϵs spectra at the $2s^2$ and $2p^2$ resonances remain stable over t_0. The latter features come from the EUV excitation of $2s2p$ and the subsequent laser transition to $2s^2$ and $2p^2$ before $2s2p$ decays. This contrast will be further investigated in view of ultrafast electron dynamics in Sec. III D.

The sidebandlike signals at $2s^2$ and $2p^2$ extend in the time delay up to $t_0 = 15$ fs. The formation of the sideband pattern corresponds to two ionization pathways—the direct EUV ionization to $1s\epsilon p$, and the EUV + VIS ionization through $2s2p$. Thus the sidebands at both $2s^2$ and $2p^2$ vanish

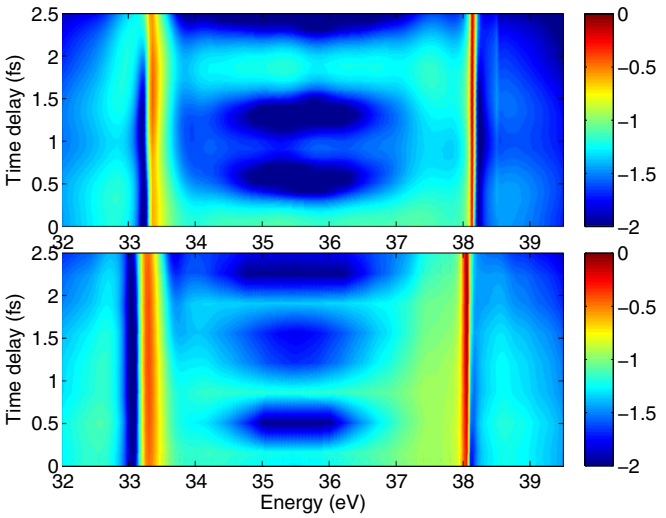

FIG. 5. (Color online) Transient electron spectra for $t_0 = 0$–2.5 fs of the s partial waves by the TAE-TDSE calculations (top panel) and the present model (bottom panel), in logarithmic scale and in 20-dB dynamic range. The strength of the middle flat part of the spectrum oscillates with t_0 in the period of half optical cycle and is weakened as the laser pulse lags behind the EUV pulse, but the resonance parts sustain over large time delays.

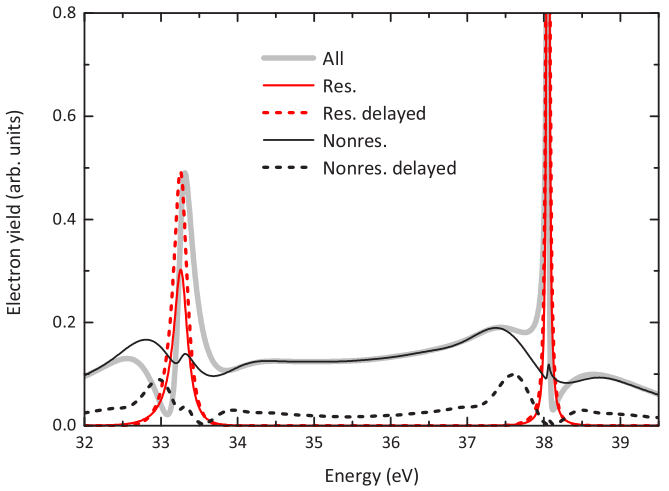

FIG. 6. (Color online) Electron spectra of the s partial wave for three sets of dipole matrix elements by the model calculation. The first set includes all the dipole matrix elements, while the second and the third sets include just the nonresonant (C-C) and just the resonant dipole matrix elements (B-B and B-C), respectively. The peak laser intensity is fixed at 1 TW/cm^2. The EUV either overlaps the laser peak or leads in time by 3 fs.

as t_0 approaches the $2s2p$ decay lifetime (17 fs), where the second ionization pathway effectively stops. The slopes of the tilted fringes on both resonances change along t_0, which are controlled by the phase differences between $2s2p$ and $2s^2$ and between $2s2p$ and $2p^2$, respectively, in the duration after the EUV excitation and before the VIS kicks in. This feature of tilted fringes has been explained by several attosecond ionization studies [32–34].

D. Short-time behavior of C-C coupling

At $t_0 = 0$, the effective bandwidth of the laser that corresponds to the dynamics of the wave packet initiated by the EUV pump is 0.9 eV. Considering this laser bandwidth, the signals in 34–37 eV of the ϵs spectrum, shown in Figs. 3 and 5, are only from the laser coupling with the $1s\epsilon p$ background continuum instead of with the $2s2p$ state. While the C-C dipole matrix elements are fixed values with the atomic structure, the signals in 34-37 eV vary closely with the laser field in t_0, as shown in Fig. 5, i.e., when the EUV pulse is on top of the local peaks of the laser field, the signals are strong, and when the EUV pulse is at the zero field of the laser, the signals attenuate. Such behavior suggests that the C-C transition is only significant at the beginning of the EUV ionization when the electrons are still at the neighborhood of the atomic core. On the other hand, the excitation of $2s2p$ lasts long after the EUV pulse, and thus the B-B coupling between $2s2p$ and $2s^2$ or $2p^2$ is insensitive to the time delay between the laser and EUV pulses.

To elucidate the role of the C-C coupling responsible for signals in 34-37 eV in the ϵs and ϵd spectra, beside the full model calculation with all the original retrieved dipole matrix elements (described in Sec. III B), we made two extra calculations with only the nonresonant (C-C) and only the resonant (B-B and B-C) ones, respectively, for $t_0 = 0$ and 3 fs. The $t_0 = 3$ fs case is for non-overlapping pulses where the laser comes later than the EUV. The resultant ϵs electron spectra are plotted in Fig. 6. In the nonresonant, $t_0 = 0$ case, the spectrum reproduces the 34–37 eV part of the full calculation very well. At $2s^2$ and $2p^2$, the resonance peaks shrink to two slight bumps, which are the results of the configuration interaction to the continuum. When the laser is delayed to $t_0 = 3$ fs, the overall nonresonant signals drop dramatically, where the bumps at 33 and 37.6 eV indicate the "actual bandwidth" 0.5 eV of the laser. The effect of the C-C coupling is substantial only if the two pulses overlap, or more specifically, the EUV overlaps the local maximum of the laser field, where the EUV-excited continuum electrons can be driven by the laser. On the contrary, in the resonant case, the flat part remains 0, and the $2s^2$ and $2p^2$ peaks retain. The bandwidth of the laser slightly changes the line widths of the resonances, but it has no effect on the empty spectral range in 34–37 eV.

The short-time behavior of the photoelectrons described above can be alternatively explained and reaffirmed by analyzing the motion of the electron wave packet in the coordinate space. Determined by the EUV, the wave packet has the central kinetic energy around $2s2p$ at 35.6 eV, corresponding to the velocity of 67 a.u./fs and the momentum of $k_0 = 1.6$ a.u. For photoelectrons along, the asymptotic condition of the continuum wave is determined by $kr \gg 1$, and the "core" size of the system can be defined by $1/k_0 = 0.6$ a.u. For bound electrons, the core size can be defined by the bound orbitals, which are less than 1 a.u. for $n \leqslant 2$. Within the core range, the emitted electrons still have the chance to interact with each other or with bound electrons. Considering the core size and the average velocity, it takes less than 20 as for the wave packet to leave the core, which is significantly shorter than the 0.9-fs half optical cycle of the laser. In other words, the photoelectrons right after the EUV ionization are boundlike only instantly in

terms of a laser optical cycle before they dissipate away. As a result, in Fig. 5, the 34–37 eV signals follow the instantaneous intensity of the laser closely. Meanwhile the excited $2s2p$ state holds electrons in the timescale of tens of femtoseconds where the laser couples $2s2p$ to the surrounding of $2s^2$ and $2p^2$, e.g., at 37.5 eV, which shows the slow attenuation of signals along t_0.

The above demonstration shows that the C-C transition in the coupled autoionizing systems is nonnegligible even in moderately intense fields, in a short period of time after the ionizing pulse. This is in contrast to the common assumption in previous studies to neglect C-C transitions when applying long pulses [35–38] and ultrashort pulses [11,18,19]. By fitting the model to the TAE-TDSE result, the C-C dipole matrix elements $D_{1s\epsilon p,1s\epsilon s}$ and $D_{1s\epsilon p,1s\epsilon s}$ are determined to be about 1 a.u./eV. This quantity is equivalent to a 0.1-a.u. dipole matrix element between the discrete states of the same widths of $2s2p$ and $2s^2$, which is 15 times smaller $D_{2s2p,2s^2}$.

IV. CONCLUSIONS

A general technique has been developed and tested to retrieve the properties of the DFRs in the autoionization region. An IAP with a synchronized short dressing pulse are applied to an atomic system to obtain the photoelectron spectra. The simulations are carried out by a multilevel model and a TAE-TDSE program, where their comparison characterizes the DFRs, in particular the dipole matrix elements of the transitions involving DFRs. Ultrafast technology is critical in this technique for the broadband excitation to cover the resonance region in concern. The multilevel model successfully recovers the electron wave packet for laser intensities up to 1 TW/cm^2. Surprisingly, it shows that the C-C transition by the laser coupling contributes significantly in the photoelectron spectra when the laser overlaps the EUV pulse. It indicates the correlation effect between the "free" photoelectrons before they move away from the core, in comparison with the bound-state coupling that has been well studied in laser-dressed systems. The effect depends on the proximity between the electrons and is controlled by the timing of the laser pulse. The general technique developed here would help the identification and characterization of DFRs for applications involving multiphoton processes, and would utilize the most advanced ultrafast optical technologies in atomic and molecular studies. An algorithm to automatically optimize the DFR parameters could be developed in the future.

ACKNOWLEDGMENTS

This work was supported in part by Chemical Sciences, Geosciences, and Biosciences Division, Office of Basic Energy Sciences, Office of Science, US Department of Energy. T.M. was supported by Grants-in-Aid for Scientific Research (A), (B), and (C) from the Ministry of Education, Culture, Sports, Science and Technology, Japan.

[1] S. E. Harris, J. E. Field, and A. Imamoglu, Phys. Rev. Lett. **64**, 1107 (1990).
[2] M. Fleischhauer, A. Imamoglu, and J. P. Marangos, Rev. Mod. Phys. **77**, 633 (2005).
[3] I. D. Abella, Phys. Rev. Lett. **9**, 453 (1962).
[4] M. Rumi and J. W. Perry, Adv. Opt. Photon. **2**, 451 (2010).
[5] M.-F. Lin, A. N. Pfeiffer, D. M. Neumark, S. R. Leone, and O. Gessner, J. Chem Phys. **137**, 244305 (2012).
[6] S. Chen, M. J. Bell, A. R. Beck, H. Mashiko, M. Wu, A. N. Pfeiffer, M. B. Gaarde, D. M. Neumark, S. R. Leone, and K. J. Schafer, Phys. Rev. A **86**, 063408 (2012).
[7] Z. H. Loh, C. H. Greene, and S. R. Leone, Chem. Phys. **350**, 7 (2008).
[8] C. Ott, A. Kaldun, P. Raith, K. Meyer, M. Laux, Y. Zhang, S. Hagstotz, T. Ding, R. Heck, and T. Pfeifer, arXiv:1205.0519.
[9] C. Ott, A. Kaldun, P. Raith, K. Meyer, M. Laux, J. Evers, C. H. Keitel, C. H. Greene, and T. Pfeifer, Science **340**, 716 (2013).
[10] U. Fano, Phys. Rev. **124**, 1866 (1961).
[11] H. Wang, M. Chini, S. Chen, C.-H. Zhang, Y. Cheng, F. He, Y. Wu, U. Thumm, and Z. Chang, Phys. Rev. Lett. **105**, 143002 (2010).
[12] S. Gilbertson, M. Chini, X. Feng, S. Khan, Y. Wu, and Z. Chang, Phys. Rev. Lett. **105**, 263003 (2010).
[13] W.-C. Chu and C. D. Lin, J. Phys. B: At. Mol. Opt. Phys. **45**, 201002 (2012).
[14] M. Wickenhauser, J. Burgdörfer, F. Krausz, and M. Drescher, Phys. Rev. Lett. **94**, 023002 (2005).
[15] Z. X. Zhao and C. D. Lin, Phys. Rev. A **71**, 060702(R) (2005).
[16] W.-C. Chu, S.-F. Zhao, and C. D. Lin, Phys. Rev. A **84**, 033426 (2011).
[17] W.-C. Chu and C. D. Lin, Phys. Rev. A **85**, 013409 (2012).
[18] A. N. Pfeiffer and S. R. Leone, Phys. Rev. A **85**, 053422 (2012).
[19] W.-C. Chu and C. D. Lin, Phys. Rev. A **87**, 013415 (2013).
[20] J. Zhao and M. Lein, New J. Phys. **14**, 065003 (2012).
[21] M. Tarana and C. H. Greene, Phys. Rev. A **85**, 013411 (2012).
[22] L. Argenti, C. Ott, T. Pfeifer, and F. Martín, arXiv:1211.2526v1.
[23] T. Morishita, K. Hino, T. Edamura, D. Kato, S. Watanabe, and M. Matsuzawa, J. Phys. B: At. Mol. Opt. Phys. **34**, L475 (2001).
[24] A. Hishikawa, M. Fushitani, Y. Hikosaka, A. Matsuda, C.-N. Liu, T. Morishita, E. Shigemasa, M. Nagasono, K. Tono, T. Togashi, H. Ohashi, H. Kimura, Y. Senba, M. Yabashi, and T. Ishikawa, Phys. Rev. Lett. **107**, 243003 (2011).
[25] C.-N. Liu, A. Hishikawa, and T. Morishita, Phys. Rev. A **86**, 053426 (2012).
[26] J. Itatani, F. Quéré, G. L. Yudin, M. Yu. Ivanov, F. Krausz, and P. B. Corkum, Phys. Rev. Lett. **88**, 173903 (2002).
[27] B. H. Bransden and C. J. Joachain, *Physics of Atoms and Molecules* (Addison-Wesley, Boston, 2003).
[28] M. Domke, K. Schulz, G. Remmers, G. Kaindl, and D. Wintgen, Phys. Rev. A **53**, 1424 (1996).
[29] D. H. Oza, Phys. Rev. A **33**, 824 (1986).
[30] Y. K. Ho, Phys. Rev. A **34**, 4402 (1986).
[31] E. Lindroth, Phys. Rev. A **49**, 4473 (1994).
[32] N. N. Choi, T. F. Jiang, T. Morishita, M.-H. Lee, and C. D. Lin, Phys. Rev. A **82**, 013409 (2010).

[33] J. Mauritsson, T. Remetter, M. Swoboda, K. Klünder, A. L'Huillier, K. J. Schafer, O. Ghafur, F. Kelkensberg, W. Siu, P. Johnsson, M. J. J. Vrakking, I. Znakovskaya, T. Uphues, S. Zherebtsov, M. F. Kling, F. Lépine, E. Benedetti, F. Ferrari, G. Sansone, and M. Nisoli, Phys. Rev. Lett. **105**, 053001 (2010).

[34] K. T. Kim, D. H. Ko, J. Park, N. N. Choi, C. M. Kim, K. L. Ishikawa, J. Lee, and C. H. Nam, Phys. Rev. Lett. **108**, 093001 (2012).

[35] P. Lambropoulos and P. Zoller, Phys. Rev. A **24**, 379 (1981).

[36] H. Bachau, P. Lambropoulos, and R. Shakeshaft, Phys. Rev. A **34**, 4785 (1986).

[37] L. B. Madsen, P. Schlagheck, and P. Lambropoulos, Phys. Rev. Lett. **85**, 42 (2000).

[38] S. I. Themelis, P. Lambropoulos, and M. Meyer, J. Phys. B: At., Mol. Opt. Phys. **37**, 4281 (2004).